Supporting Information

Cu_2In/In core-shell interface regulating $Cu^{0/+}$ enables selective *OCHO capture for efficient CO_2-to-formate conversion across a wide potential range

*Ziya Li [a], Caixia Chi [b], Gaoqiang Zhao [a], Qiuyue Zhang [a], Zhiguo Lv [a], Feng Wang [c], Tao Zhuang [d] and Chao Zhang [a] **

[a] *State Key Laboratory Base for Eco-chemical Engineering, College of Chemical Engineering, Qingdao University of Science and Technology, Qingdao 266042, China*

[b] *Heilongjiang Province Key Laboratory of Environmental Catalysis and Energy Storage Materials, Food and Pharmaceutical Engineering, Suihua University, Suihua 152061, China*

[c] *Shandong Provincial Key Laboratory of Monocrystalline Silicon Semiconductor Materials and Technology, Dezhou University, Dezhou 253023, China*

[d] *Key Laboratory of Rubber-Plastics, Ministry of Education/Shandong Provincial Key Laboratory of Rubber-plastics, Qingdao University of Science & Technology, Qingdao 266042, China*

*Corresponding author:

E-mail: chaozhangchem@qust.edu.cn (Chao Zhang)

Material characterization

The morphologies of samples were observed by Scanning electron microscopy (SEM, Hitachi S-4800). Transmission electron microscopy (TEM) and high-resolution TEM (HRTEM) measurements were performed on JEM-2100UHR with operating at 200 kV. The elemental compositions of the catalyst were studied by EDS. The Cu K-edge XAFS spectrum was collected in the mode of transmission and discussed by IFEFFIT program. The crystal structure of all samples was recorded by X-ray diffraction (XRD) on ULTIMA IV (Rigaku Corporation) with Cu-Kα radiation, the range of 2 Theta from 10 to 90°, 40 kV of rated voltage and 40 mA of rated current. The X-ray photoelectron spectra (XPS) measurements were carried out using Thermo ESCALAB 250 instruments (USA) with non-monochromatic Al Kα 1486.6 radiation. N_2 adsorption-desorption isotherms were recorded on a Micromeritics ASAP 2460 analyzer to assess the catalyst's pore architecture and surface area. Prior to measurement, each sample was degassed under vacuum at 200 °C for 3 h. The Brunauer-Emmett-Teller (BET) equation was applied to calculate the specific surface area and average pore diameter. The total pore volume was obtained from a single-point adsorption at a relative pressure of ≈0.99, and the micropore volume was determined by the t-plot method. X-ray absorption spectra at the Cu K-edge were collected at the 4B9A beamline of the AnHui Synchrotron Radiation Facility (BSRF). All XANES and EXAFS data were processed and analyzed using Athena and Artemis software. The confocal Raman microscope system (Horiba, RAMAN Solie) was equipped with a 532 nm (He-Ne laser) laser source, a semiconductor-cooled charge-coupled device (CCD)

detector (1024 × 800 pixels), a 50 μm confocal pinhole, and a 50× objective lens (NA = 0.50, 10.6 mm), which was used in this study. Standard single-point calibration was performed using a silicon line (520.5 cm^{-1}). The laser power was set to 1.2 mW, with an integration time of 0.5 seconds per point and three repeated scans. Each sample was tested with three repetitions. The IR spectra were recorded on a Bruker verter70 Fourier transform infrared (FTIR) Spectrometer within the 450-4000 cm-1 region.

CO_2RR electrochemical measurements

The electrochemical characterization was performed in an H-cell configuration at ambient temperature using an electrochemical workstation (CHI 660E, CH Instruments, China). For CO_2RR measurements, a 0.5 M $KHCO_3$ solution was used as the electrolyte. A Nafion N117 membrane was employed to separate the compartments of the H-cell in electrocatalytic CO_2 reduction experiments. The reference electrode used in the electrolyte was a saturated calomel electrode (SCE). Platinum sheets were used as the counter electrode, and the self-supported catalysts were directly connected to the working electrode. The flow rate of CO_2 gas was set as ~ 20 $mL \cdot min^{-1}$.

Due to activity factors, we measured the pH of the 0.5 M $KHCO_3$ aqueous solution, which was 8.4. Electrode potentials recorded in the 0.5 M $KHCO_3$ electrolyte were calibrated to the reversible hydrogen electrode (RHE) reference scale using the Nernst equation, which is expressed as:

$$E\,(vs.\,RHE) = E\,(vs.\,SCE)) + 0.241\,V + 0.0591 \times pH \quad (1)$$

Product analysis: The gas -phase products were detected using online gas chromatograph (GC 7920) equipped with a thermal conductivity detector and a flame

ionization detector. Liquid products were quantified by 1H nuclear magnetic resonance (NMR) spectroscopy (JEOL- 400YH 400 MHz) through a water suppression mode. The following equation was used to determine the Faradaic efficiency of any gas or liquid product:

$$FE = \frac{znF}{Q} \times 100\% \quad (2)$$

where z denotes the number of transferred electrons, n represents the amount of substance (in moles) of the gaseous or liquid reduction products, F is Faraday's constant, and Q refers to the total electric charge applied during the CO_2 reduction process. To quantify the partial current densities of the CO_2RR products and H_2, the following equation was employed:

$$jpartial\ current\ density = jtotal \times FE/S \quad (3)$$

In this equation, j_{total} refers to the total current, FE represents the Faradaic efficiency obtained from Equation (2), and S represents the geometric area of the cathode.

In 0.5 M $KHCO_3$ aqueous solution, we consider reaction paths for CO_2RR and HER as following:

CO_2RR:

$$CO_2 + H^+ + e^- + * \rightarrow *OCHO\ (1)$$

$$*OCHO + H^+ + e^- + * \rightarrow HCOOH\ (2)$$

HER:

$$H_2O + e^- \rightarrow H* + OH^-\ (1)\ \text{Volmer step}$$

$$H_2O + e^- + H* \rightarrow H_2 + OH^-\ (2)\ \text{Heyrovsky step}$$

$$H* + H* \rightarrow H_2\ (3)\ \text{Tafel step}$$

DFT calculations detail

The density functional theory (DFT) calculation was carried out using the Cambridge serial total energy package (CASTEP) code, in which a plane wave basis set was used. The model was established by the generalized gradient approximation (GGA) and the Perdew-Burke-Ernzerhof (PBE) functional. The cutoff energy of the OTFG ultrasoft pseudopotential was 550 eV. The Brillouin zone integration was performed using 3×3×1 k-point sampling through all the computational process. Geometric convergence tolerances with maximum force and maximum displacement were 0.03 eV/Å and 10^{-3} Å. The self-consistent field (SCF) tolerance was set to a high accuracy of 10^{-6} eV/atom for energy convergence. The plane-averaged charge density difference (Δρ) along the Z-direction was calculated to investigate the interfacial electronic redistribution in the Cu2In/In core-shell structure. The differential charge density was obtained using the following expression:

$$\Delta\rho(r) = \rho Cu_2In/In(r) - \rho Cu_2In(r) - \rho In(r) \quad (1)$$

where $\rho Cu_2In/In(r)$ is the total charge density of the combined system, and $\rho Cu_2In(r)$ and $\rho In(r)$ are the charge densities of the isolated Cu_2In core and In shell, respectively, calculated under the same atomic configurations as in the full system.

To quantify the interfacial charge redistribution, the plane-averaged charge density difference along the Z-axis was derived by integrating over the x-y plane:

$$\Delta\rho(z) = (1/A) \iint \Delta\rho(x, y, z)\, dx\, dy \quad (2)$$

The adsorption energy of X (where X is H_2O, CO_2, HCOOH, H, OH, OCHO) on catalysts is determined as:

$$\Delta EX = EX/surf - EX - Esurf \quad (3)$$

where $E_{X/surf}$, E_X and E_{surf} are the total energies of the surface with the X adsorbate, the energy of the X and the energy of clean surfaces of catalysts, respectively.

Thermodynamic free energies were obtained as:

$$G = EDFT + EZPE - TS \quad (4)$$

where E_{DFT} is the DFT ground state, E_{ZPE} is the zeropoint energy, and S is the entropy.

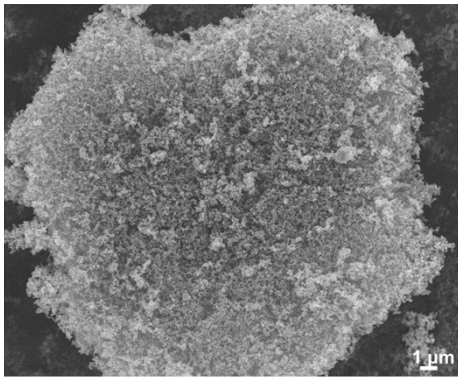

Fig. S1. SEM image for Cu_2In/In.

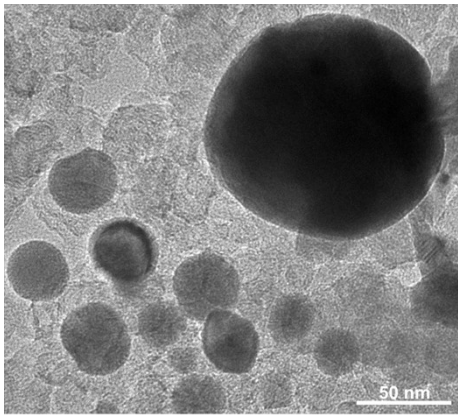

Fig. S2. The TEM image of Cu_2In/In.

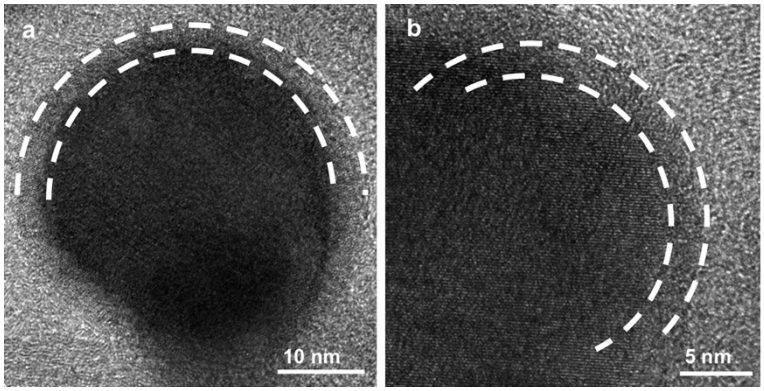

Fig. S3. (a-b) The HR-TEM of Cu_2In/In.

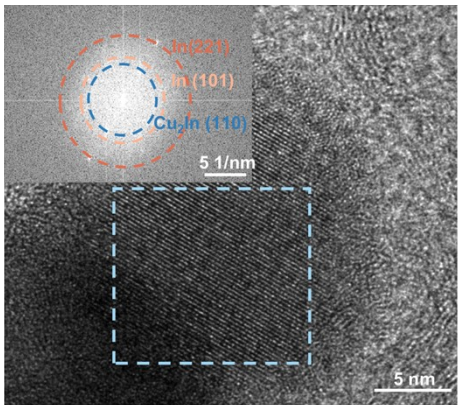

Fig. S4. The HR-TEM image of Cu_2In/In showing lattice fringes, along with Fast Fourier Transform (FFT) of the electron diffraction pattern.

Fig. S4 reveals the presence of the (110) plane of Cu_2In along with the (101) and (221) planes of In.

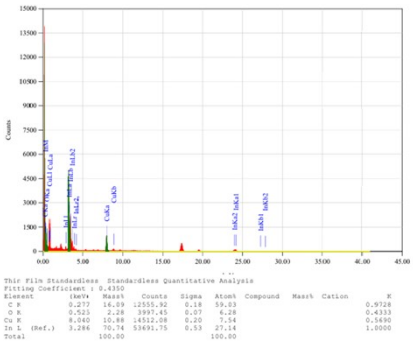

Fig. S5. The quantitative analysis of Cu_2In/In was performed using EDS.

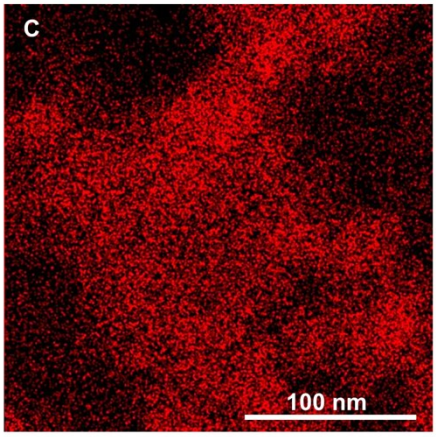

Fig. S6. STEM-EDS mapping of the Cu_2In/In catalyst showing the distributions of C.

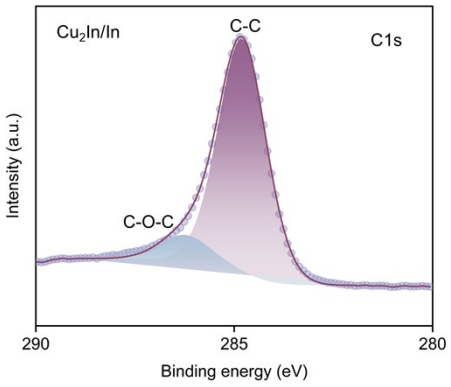

Fig. S7. High-resolution XPS profiles of C 1s of Cu_2In/In. The C 1s spectrum of Cu_2In/In shows the corresponding characteristic peaks of C-C and C-O.

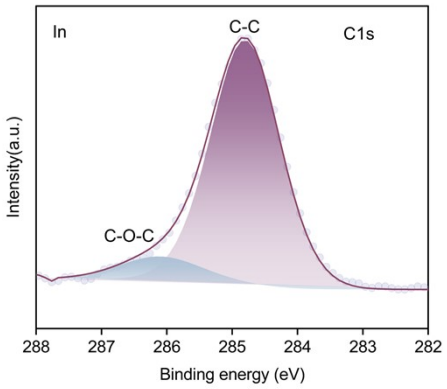

Fig. S8. High-resolution XPS profiles of C 1s of In. The C 1s spectrum of In shows the corresponding characteristic peaks of C-C and C-O.

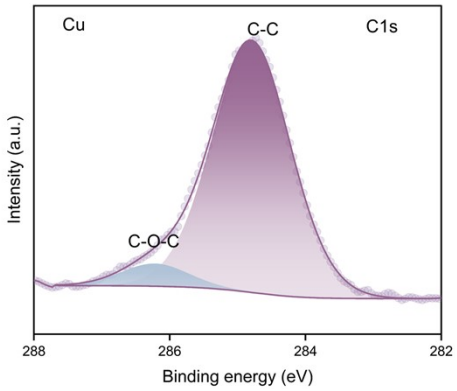

Fig. S9. High-resolution XPS profiles of C 1s of Cu. The C 1s spectrum of Cu shows the corresponding characteristic peaks of C-C and C-O.

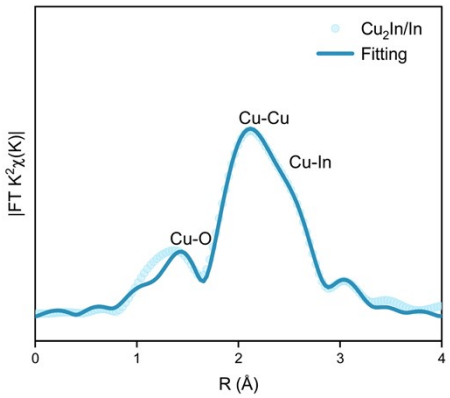

Fig. S10. EXAFS R-space fitting results of Cu_2In/In.

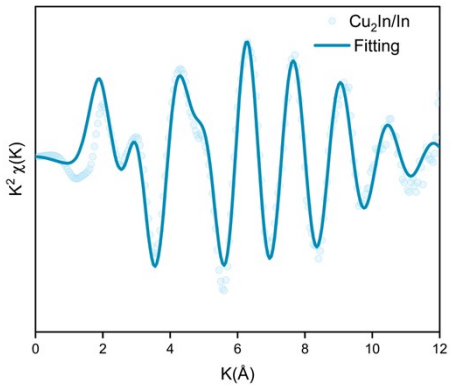

Fig. S11. EXAFS K-space fitting results of Cu_2In/In.

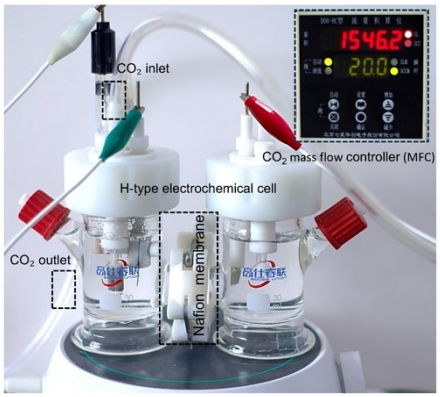

Fig. S12. Photograph of the H-type electrochemical cell used for CO_2 electroreduction. The two compartments are separated by a Nafion membrane. CO_2 gas is introduced into the cathodic chamber via a CO_2 mass flow controller (MFC) at a flow rate of 20 mL min^{-1}. The CO_2 inlet and outlet are indicated. The entire setup is placed on a magnetic stirrer to ensure homogeneous mixing during electrolysis.

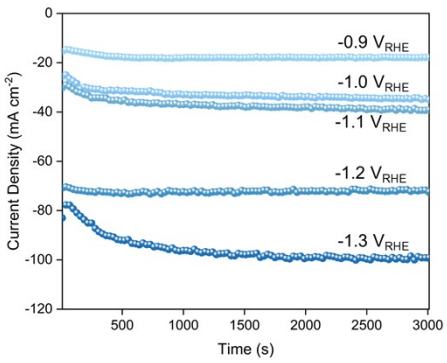

Fig. S13. Chronoamperometric measurements (i-t curves) of the Cu_2In/In catalysis.

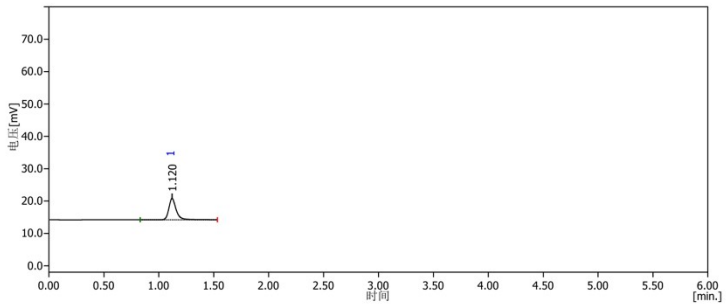

序号	组份名称	保留时间	峰面积	浓度:	面积百分比	浓度百分比
1		1.12	30.6883		100.0000%	
合计			30.6883	0.0000	100%	0.0000

Fig. S14. Gas chromatogram (GC) of hydrogen for Cu_2In/In.

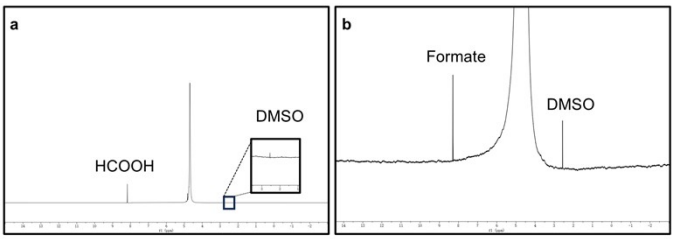

Fig. S15. ^{1}H Nuclear Magnetic Resonance (^{1}H NMR) Spectrum of (a) Pure Formic Acid, and (b) electrolyte after reaction with Cu_2In/In.

In order to identify the liquid-phase products present in the electrolyte, liquid-state ^{1}H NMR spectroscopy was performed on a commercial formic acid sample. The obtained spectra enabled precise identification and analysis of the hydroxyl proton signal within the molecular structure.

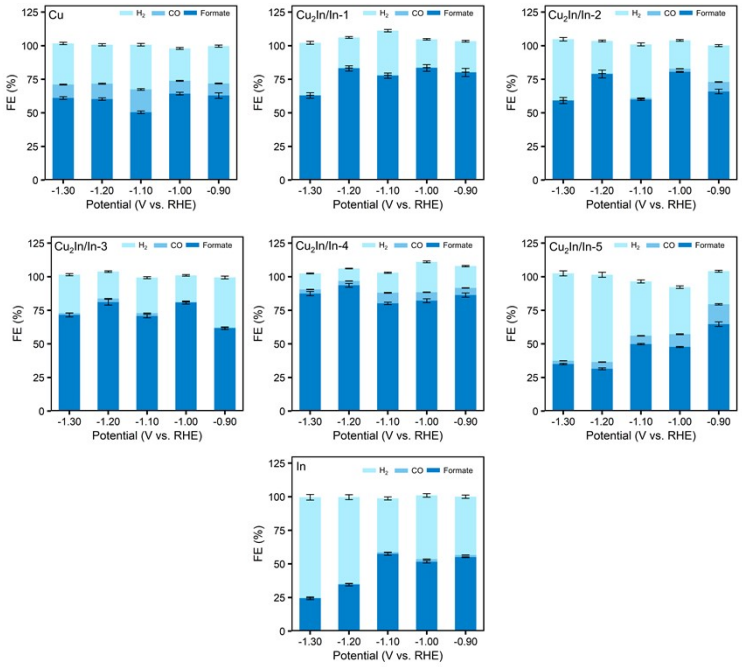

Fig. S16. Faradaic Efficiency of Cu, Cu_2In/In-x (x=1, 2, 3, 4, 5), and In.

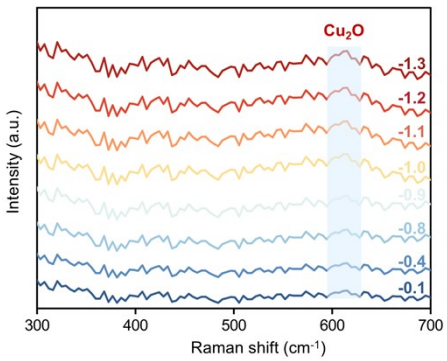

Fig. S17. In situ Raman spectra of Cu. Electrochemical measurements were carried out in 0.5M KHCO3 electrolyte at a potential referenced to the reversible hydrogen electrode (RHE).

In-situ Raman testing reveals a peak at 611 cm^{-1}, attributed to Cu (I) oxide, further confirming the presence of $Cu^{0/+}$ mixed valence in our catalyst. [1,2]

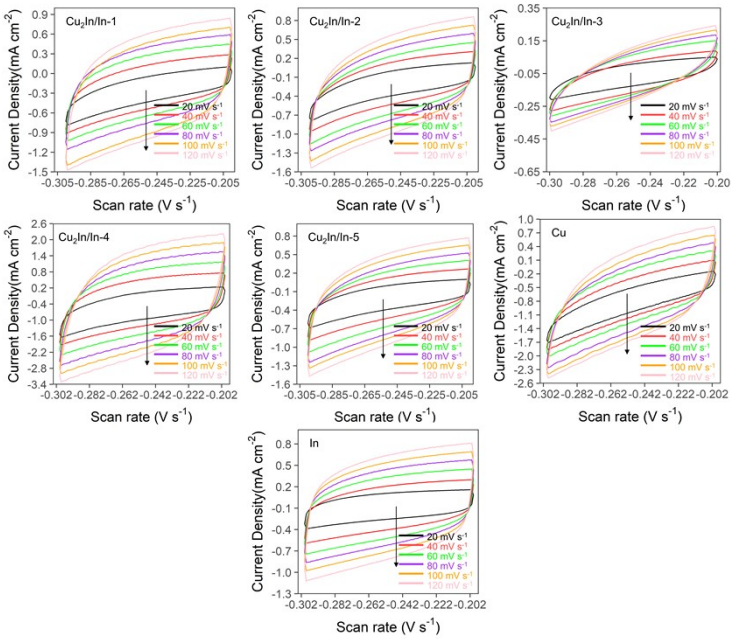

Fig. S18. CV curves of Cu, Cu_2In/In-x (x=1, 2, 3, 4, 5), and In.

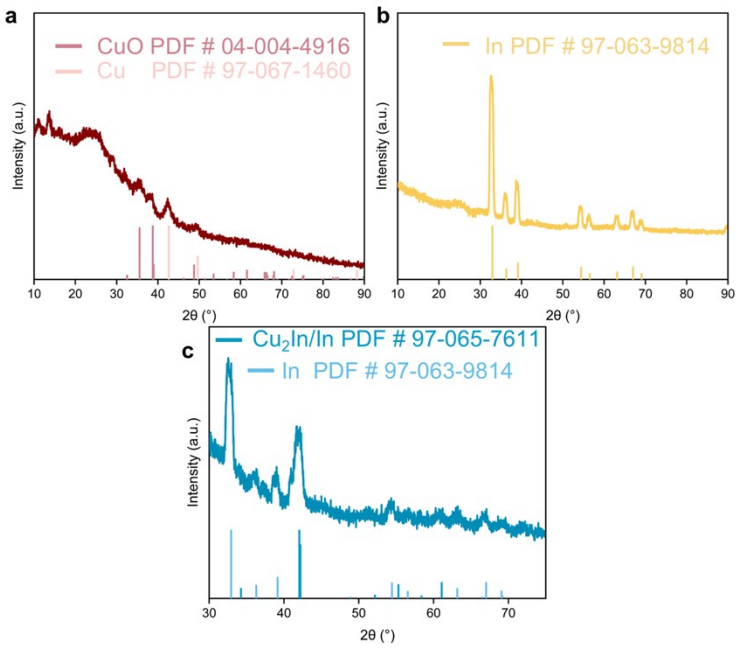

Fig. S19. XRD patterns of the (a) Cu, (b) In, (c) Cu_2In/In catalyst after CO_2RR testing.

As shown in Fig. a, the post-reaction Cu sample exhibits a strong CuO signal, indicating that the copper surface has undergone oxidation. No oxide-related peaks are observed on the In surface, and the Cu_2In core, encapsulated by the In shell, shows no significant signals corresponding to oxidation states. The absence of significant oxidation state changes of In before and after the reaction confirms its excellent chemical stability. As shown in Fig. c, when In is incorporated into the core-shell structure, the In shell enhances the catalyst's resistance to oxidation and preserves the active interface. This is further confirmed by the retention of the Cu_2In phase and the structural integrity of the catalyst, with no significant phase transformation or new impurity peaks observed, indicating outstanding structural stability under electrochemical operating conditions.

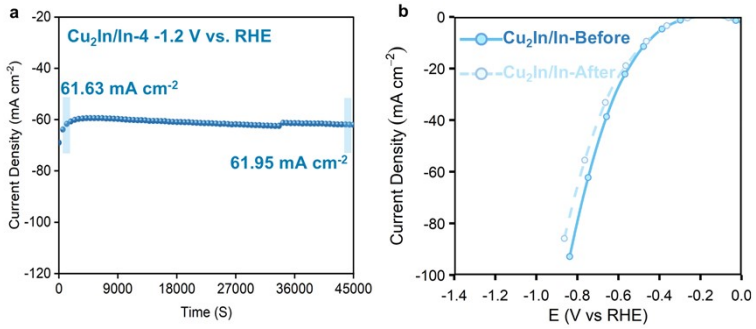

Fig. S20. (a) Stability at −1.2 V vs. RHE working voltage for 13 h. (b) LSV curves before and after the 13 h stability test at −1.2 V vs. RHE.

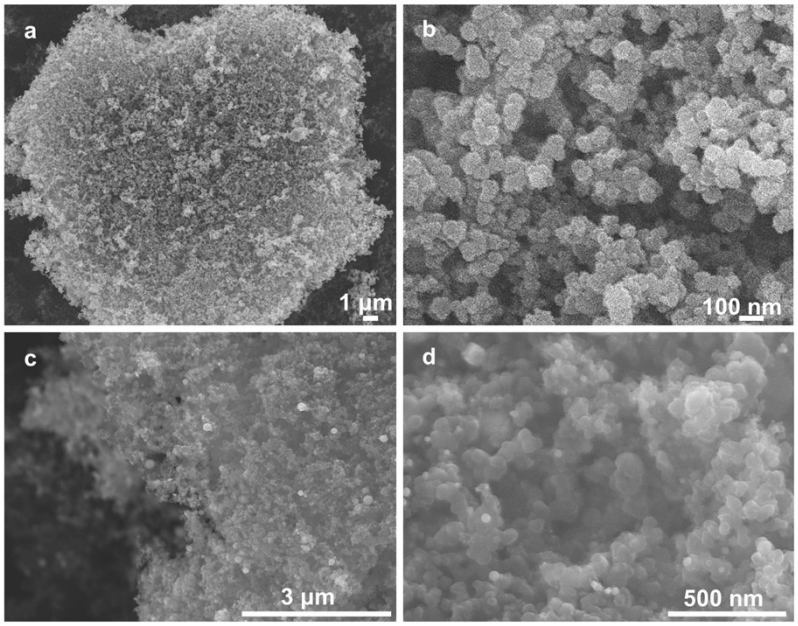

Fig. S21. (a-b) SEM images before the reaction, (c-d) SEM images after the reaction.

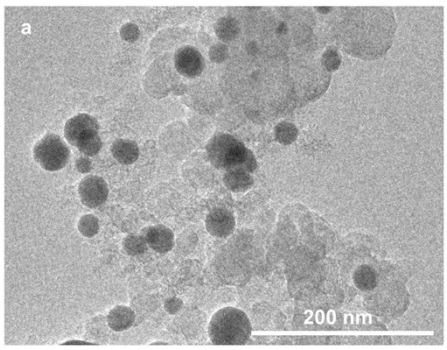

Fig. S22. TEM images after the reaction of Cu_2In/In.

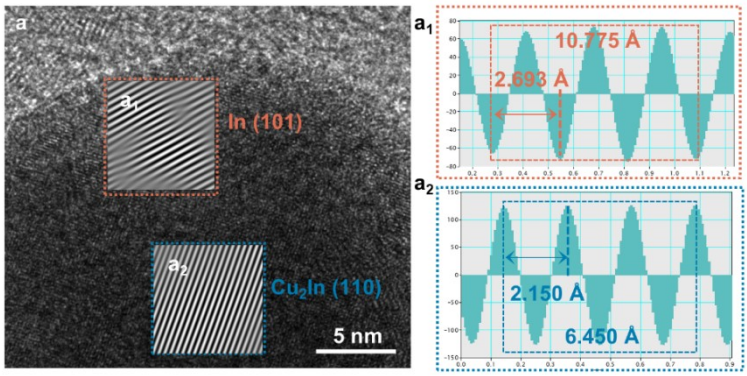

Fig. S23. (a) HR-TEM images after the reaction of Cu_2In/In. (a_1) and (a_2) correspond to the lattice fringes observed in the Fourier-transformed image of Fig. a.

To further confirm the stability of the core-shell structure, we conducted lattice spacing analysis. The measured lattice spacings of 2.150 Å and 2.693 Å correspond to the (110) plane of Cu_2In and the (101) plane of In, respectively.

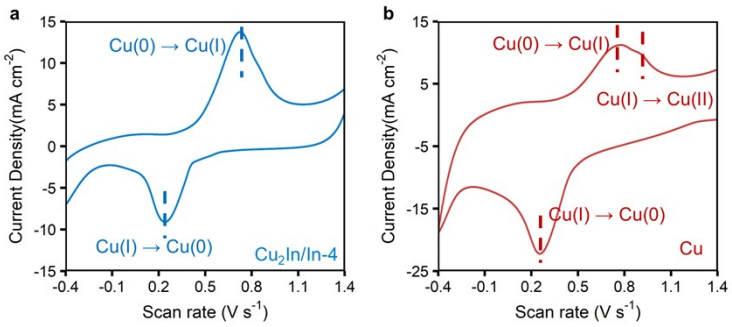

Fig. S24. CV under oxidative conditions of (a) Cu_2In/In, (b) Cu.

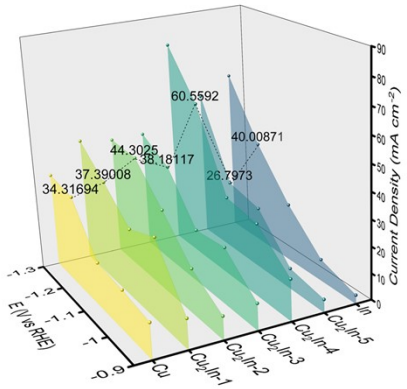

Fig. S25. Partial current density of formate production on Cu, Cu_2In/In-x (x=1, 2, 3, 4, 5), and In.

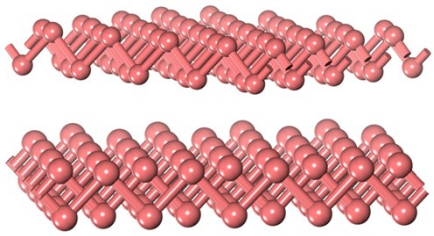

Fig. S26. The optimized structural models of In.

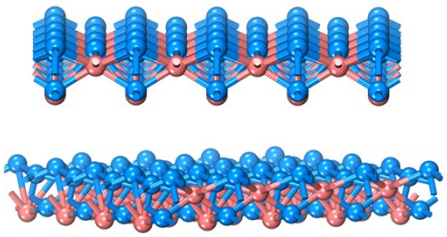

Fig. S27. The optimized structural models of Cu_2In.

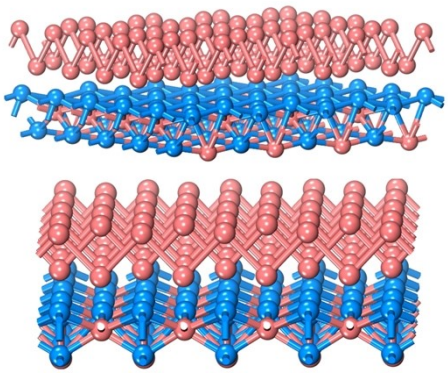

Fig. S28. The optimized structural models of Cu_2In/In.

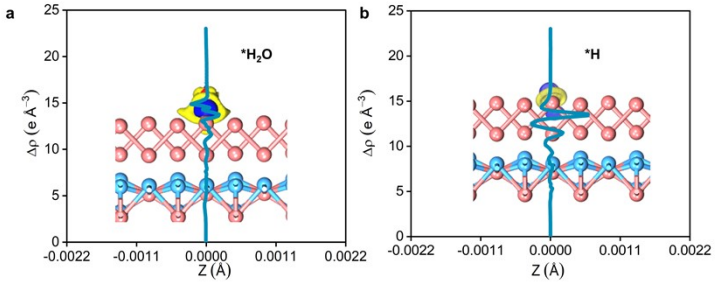

Fig. S29. Plane-averaged charge density difference (Δρ) profiles along the Z-direction and corresponding isosurface plots for (a) *H_2O and (b) *H adsorption on the Cu_2In/In interface.

The yellow and blue regions represent electron accumulation and depletion, respectively. Both *H_2O adsorption and *H adsorption induces only minor fluctuations in Δρ, reflecting weak electron redistribution and limited interaction strength at the interface. In particular, the weak stabilization of *H suggests that the Cu_2In/In interface is not favorable for the HER, thereby suppressing the competing HER pathway. These findings highlight the selective nature of the Cu_2In/In catalyst surface, which disfavors *H and *H_2O adsorption while preferentially stabilizing key CO_2RR intermediates such as *OCHO, thus enhancing the overall selectivity toward formate production.

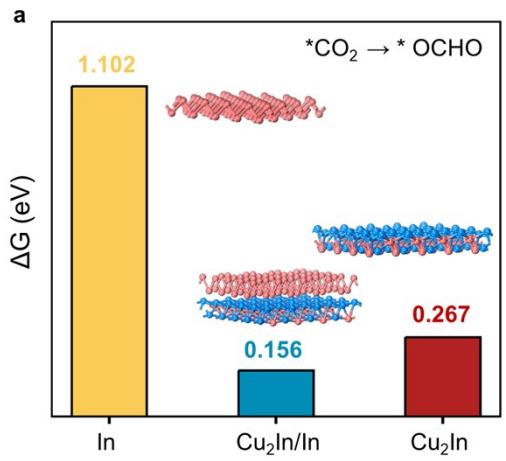

Fig. S30. (a) Free Energy Barrier (ΔG) for the Reduction of $*CO_2$ to *OCHO intermediate over In, Cu_2In, and Cu_2In/In.

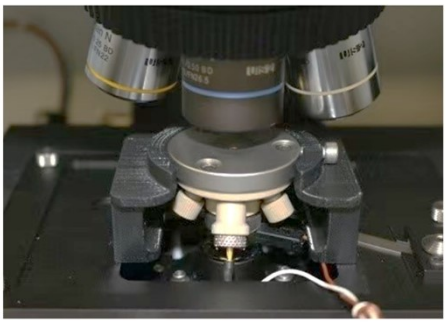

Fig. S31. Schematic of the in-situ Raman spectroscopy setup used for CO_2RR measurements.

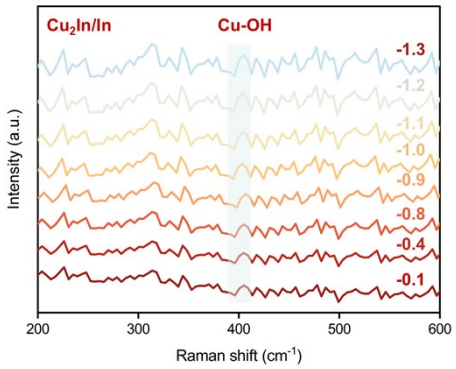

Fig. S32. (a) In situ Raman spectra of Cu_2In/In. Electrochemical measurements were carried out in 0.5M $KHCO_3$ electrolyte at a potential referenced to the reversible hydrogen electrode (RHE).

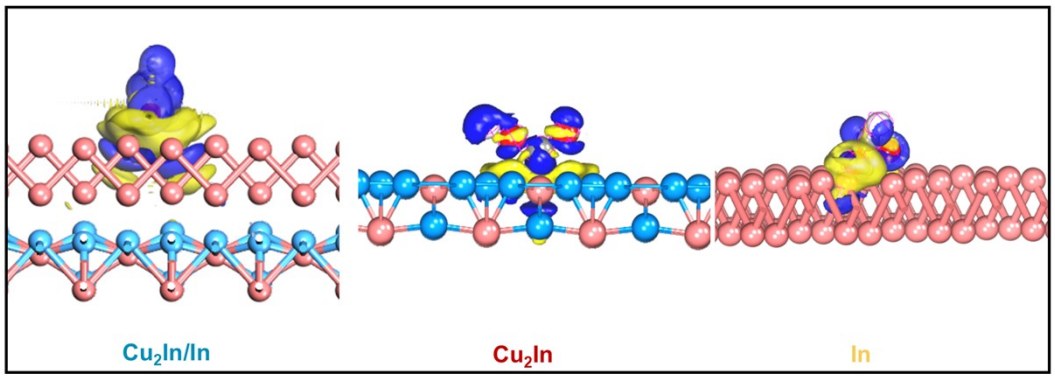

Fig. S33. (a) Free Energy Barrier (ΔG) for the Reduction of $*CO_2$ to *OCHO intermediate over In, Cu_2In, and Cu_2In/In.

Table S1. Element content of Cu_2In/In.

Sample	Element	Line	Mass%	Atom%
Cu_2In/In	C	K	16.09	59.03
	O	K	2.28	6.28
	Cu	K	10.88	7.54
	In	L	70.74	27.14
	Total		100	100

Table S2. Structural parameters extracted from the Cu k-edge EXAFS fitting. (S_0=1).

Sample	Scattering pair	CN	R(Å)	$\sigma^2(10^{-3}$ Å$^2)$	ΔE_0(eV)	R factor
Cu_2In/In	Cu-O	0.518	1.83890	8.36	-2.093	0.01845
	Cu-Cu	2.525	2.46780	11.04	-2.093	0.01845
	Cu-In	2.135	2.70870	22.36	-2.093	0.01845
	Cu-Cu	6.103	3.71740	40.22	-2.093	0.01845

CN: the coordination number; R(Å): the inter-atomic distance by fitting; σ^2: Debye-Waller factor (a measure of thermal and static disorder in absorber-scatterer distances); ΔE_0: edge-energy shift (the difference between the zero kinetic energy value of the sample and that of the theoretical model); R factor: used to value the goodness of the fitting; This value was fixed during EXAFS fitting, based on the known structure.

Table S3. Performance comparison among representative MoS_2-based catalysts reported in the literature. In this study, Cu_2In/In is the focus of catalytic investigation.

catalyst	FE $_{formate}$ (%)	Current density (mA cm^{-2})	Reference
Cu fiber felt	71 ± 3.0	——	1 [3]
Cu^{+}HAP/3D	50	——	2 [4]
$Sn_{0.75}Zn_{0.25}O_y$	69	——	3 [5]
$BiPO_4$	85	534	4 [6]
$BiFeO_3/Bi_{25}FeO_{40}$	85	160	5 [7]
$Sn_{1-X}In_X@In_{1-Y}Sn_YO_Z$	80	5.2	6 [8]
CuBr-TBA-R	84.4	——	7 [9]
$RbCu_7S_4$	90.4 ± 1.3	272.1	8 [10]
HCS/Cu-0.12	82.4	26	9 [11]
InN-C	92.2	60.1	10 [12]
$LaInO_3$	91.4	106.8	11 [13]
Cu_2In/In	93.6	64.7	own

References

1. L. Wang, Z. Chen, Y. Xiao, L. Huang, X. Wang, H. Fruehwald, D. Akhmetzyanov, M. Hanson, Z. Chen, N. Chen, B. Billinghurst, R. D. L. Smith, C. V. Singh, Z. Tan and Y. A. Wu, Stabilized $Cu^{\delta+}$-OH species on in situ reconstructed Cu nanoparticles for CO_2-to-C_2H_4 conversion in neutral media, Nat. Commun., 2024, **15**, 7477.
2. S. Chen, W. H. Li, W. Jiang, J. Yang, J. Zhu, L. Wang, H. Ou, Z. Zhuang, M. Chen, X. Sun, D. Wang and Y. Li, MOF encapsulating n-heterocyclic carbene-ligated copper single-atom site catalyst towards efficient methane electrosynthesis, Angew. Chem. Int. Ed., 2022, **61**, e202114450.
3. S. Shen, J. He, X. Peng, W. Xi, L. Zhang, D. Xi, L. Wang, X. Liu and J. Luo, Stepped surface-rich copper fiber felt as an efficient electrocatalyst for the CO_2RR to formate, *J. Mater. Chem. A*, 2018, **6**, 18960-18966.
4. M. Ferri, L. Delafontaine, S. Guo, T. Asset, P. Cristiani, S. Campisi, A. Gervasini and P. Atanassov, Steering Cu-Based CO_2RR Electrocatalysts' Selectivity: Effect of Hydroxyapatite Acid/Base Moieties in Promoting Formate Production, *ACS Energy Lett.*, 2022, **7**, 2304-2310.
5. J. Jiang, B. Huang, R. Daiyan, B. Subhash, C. Tsounis, Z. Ma, C. Han, Y. Zhao, L. H. Effendi, L. C. Gallington, J. N. Hart, J. A. Scott and N. M. Bedford, Defective Sn-Zn perovskites through bio-directed routes for modulating CO_2RR, *Nano Energy*, 2022, **101**, 107593.
6. S. Ruan, B. Zhang, J. Zou, W. Zhong, X. He, J. Lu, Q. Zhang, Y. Wang and S. Xie, Bismuth nanosheets with rich grain boundaries for efficient electroreduction of CO_2 to formate under high pressures, *Chin. J. Catal.*, 2022, **43**, 3161-3169.

7. C. Xu, Y. Wang, W. Li, D. Gao, G. Wang and R. Cai, Bismuth Iron Oxide Catalysts for Efficient CO_2 Electroreduction to Formate, *ACS Appl. Mater. Interfaces*, 2024, **16**, 39305-39311.
8. L. C. Pardo Pérez, D. Teschner, E. Willinger, A. Guiet, M. Driess, P. Strasser and A. Fischer, In Situ Formed "$Sn_{1-X}In_X$@$In_{1-Y}Sn_YO_Z$" Core@Shell Nanoparticles as Electrocatalysts for CO_2 Reduction to Formate, *Adv. Funct. Mater.*, 2021, **31**, 2103601.
9. J. Troyano, E. Zapata, J. Perles, P. Amo-Ochoa, V. Fernández-Moreira, J. I. Martínez, F. Zamora and S. Delgado, Multifunctional Copper(I) Coordination Polymers with Aromatic Mono- and Ditopic Thioamides, *Inorg. Chem.*, 2019, **58**, 3290-3301.
10. X. Cui, M. Wu, G. Hou, Y. Li, Y. Wang, Y. Wang, J. Huang, M. Zhao, Z. Z. Luo, Z. Zou, Y. Zhang and M. Shao, Alkali Metal Ions Stabilizing Copper(I)–Sulfur Bonds for Efficient Formate Production from Electrochemical CO_2 Reduction, *ACS Catal.*, 2024, **14**, 11857-11864.
11. J. Du, Y. Xin, M. Dong, J. Yang, Q. Xu, H. Liu and B. Han, Copper/Carbon Heterogenous Interfaces for Enhanced Selective Electrocatalytic Reduction of CO_2 to Formate, *Small*, 2021, **17**, 2102629.
12. P. Hou, X. Wang and P. Kang, Membrane-electrode assembly electrolysis of CO_2 to formate using indium nitride nanomaterials, *J. CO_2 Util.*, 2021, **45**, 101449.
13. Y. Zhu, W. Zhou, Z. Dong, X. Zhang, Z. Chen, Z. Liu, F. Li, J. Fan, M. Jiao and L. Liu, Nanosized $LaInO_3$ perovskite for efficient electrocatalytic reduction of CO_2 to formate, *J. CO_2 Util.*, 2023, **68**, 102342.